Fundamental- and Harmonic-Frequency Circuit-Model Analysis of Interdigital Transducers with Arbitrary Metallization Ratios and Polarity Sequences

W. RICHARD SMITH, MEMBER, IEEE, AND WILLIAM F. PEDLER, MEMBER, IEEE

Abstract—A three-port circuit model is developed that describes the operation of interdigital transducers with arbitrary metallization ratios and electrode-polarity sequences at fundamental and higher harmonic frequencies. The electric fields that excite surface acoustic waves are found on an electrode-by-electrode basis using the approximation that the local electric fields are not influenced by electrodes more distant than the next-nearest neighbors. The resultant fields are expressed in terms of familiar functions, with a "universal" set of expansion coefficients given in Appendix II. Use of these fields in the circuit model developed earlier by other authors describes arbitrary transducers by modeling each electrode using the expansion coefficients appropriate to the local electrode environment. Illustrative results include the effective coupling coefficient of single- and double-electrode transducers of arbitrary metallization ratio for frequencies up to and including the eleventh harmonic. Also included is one example of the consequences of end effects in short transducers, and a detailed comparison of theory and experiment for transducers with a nonalternating polarity sequence [phase-reversal transducers (PRT's)].

I. INTRODUCTION

THIS PAPER describes a new circuit model for interdigital transducers that accounts for the spatial distribution of the driving electric field in transducers with arbitrary metallization ratios and polarity sequences. It therefore gives a description of transducer operation at both fundamental and higher harmonic frequencies and accounts for end effects in short transducers as well as for the effects of polarity reversals in phase-reversal transducers (PRT's). The new circuit model is essentially a generalization of the crossed-field Mason-circuit model.

The crossed-field Mason-circuit model [1] has been successful in predicting many of the interesting properties of interdigital transducers. For fundamental-frequency operation, i.e., operation in a band near the synchronous frequencies of the electrodes (where the electrode spacing is one-half acoustic wavelength), the crossed-field model gives a rather accurate prediction of all the three-port scattering properties of a transducer. The accurate prediction of the acoustic reflection coefficient has been aided by the use of different acoustic-wave impedances in the electrode and gap regions to represent electrode mass/electrical loading.

Manuscript received March 3, 1975; revised May 19, 1975. This work was supported by the U.S. Army Electronics Command, Fort Monmouth, N.J., under Contract DAAB07-73-C-0175.

The authors are with the Ground Systems Group, Hughes Aircraft Company, Fullerton, Calif. 92634.

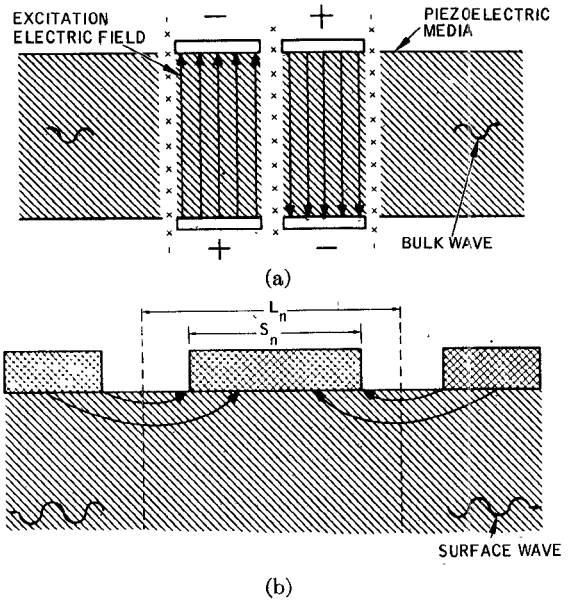

Fig. 1. Crossed-field bulk-wave model compared to surface-wave transducer geometry. (a) Crossed-field bulk-wave model used to represent an interdigital surface-wave transducer. (b) Geometry for one electrode section of an interdigital surface-wave transducer.

Because the crossed-field Mason circuit was derived for bulk waves [2], it is strictly valid for the bulk-wave electric/acoustic field distributions shown in Fig. 1(a) rather than for the surface-wave field distributions shown in Fig. 1(b). In using the crossed-field model for surface waves, we have previously made certain modifications [3] to the Mason equivalent circuit which are appropriate to the surface-wave geometry of Fig. 1(b). Specifically, for the case of single electrodes with alternating polarities, we previously calculated the electrostatic capacitance from the surface-wave field distribution of Fig. 1(b), including the effect of the metallization ratio L_n/S_n. In addition, we previously included the effects of electrode mass/electrical loading by subdividing each element[1] into Mason circuits for the electrode and gap regions. The important feature here is that the acoustic-wave admittance (Y_S) of the metallized electrode regions is slightly different from that of the gap regions (Y_G). In this circuit we used the actual metallization ratio in determining the relative acoustic-transmission-line lengths for the electrode and

[1] The term "element" refers to that portion of a transducer which consists of one electrode and the adjacent interelectrode gap.

gap portions of the corresponding Mason circuits. Furthermore, for the case of double electrodes, we further subdivided the Mason circuit so that the alternating transmission lines of wave admittances Y_S and Y_G always correspond in sequence and in length to the alternating stripes and gaps in the transducer. However, we did not calculate the exact capacitance of double electrodes as a function of the metallization ratio.

The bulk-wave Mason model has been successful for operation near acoustic synchronism because in that region, the shape of the transducer transfer functions is controlled primarily by the way in which the waves from the various electrodes interfere rather than by the frequency dependence of any one electrode. Specifically, the electroacoustic transfer function is dominated by the array factor [3], $A(\beta)$, given by

$$A(\beta) = \sum_{n=1}^{N} e_n(\beta) \exp(-j\beta x_n). \quad (1)$$

Here β is the wavenumber, x_n is the spatial position of the nth electrode, N is the number of electrodes, and $e_n(\beta)$ is the *element factor* of the nth electrode. The element factor is the Fourier transform of some appropriate field quantity which is taken as the source term for acoustic waves under one electrode. It is a slowly varying function of the wavenumber β compared to the transducer array factor $A(\beta)$. In the crossed-field Mason bulk-wave model, this source field is taken as $d/dx(E_z)$ where E_z is the electric field component normal to the surface, and x is the direction of propagation along the surface. Since this source field consists of a pair of delta functions for the Mason circuit, the crossed-field Mason-circuit model is closely related [3] to the delta-function model [4] and impulse model [5].

It is the slowly varying element factor $e_n(\beta)$ that is inaccurate when using the Mason circuit, delta-function model, or impulse model to describe surface-wave transducers. Since an inaccurate electric field distribution (usually independent of the metallization ratio) is used, the element factor incurs severe errors at frequencies far removed from acoustic synchronism, and any of the foregoing models is incapable of describing overtone operation. In addition, end effects in short transducers, nonalternating polarity sequences, and the double-electrode [6], [7] geometry are not adequately described.

The present work overcomes these difficulties by combining features of several previous analyses. Some of these contained the appropriate electric field distribution or element factor for specific geometries but lacked the complete three-port transfer function description of a circuit model approach. In the important early work by Engan [8], the proper electric field distribution was found for an infinite array of single electrodes. More recently, Hartmann and Secrest [9] developed a computer program which uses an iterative procedure to find the electric fields for a transducer consisting of a finite number of electrodes of arbitrary width and spacing, with an arbitrary uniform potential specified on each electrode. Using this program,

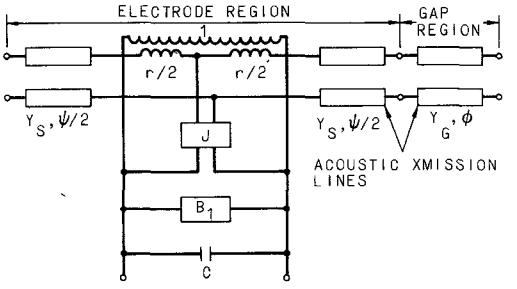

Fig. 2. Equivalent circuit model for one electrode and adjacent gap in an interdigital transducer.

they presented the spectra of a source term for acoustic waves, giving as examples the harmonic content for an infinite array of double electrodes and the reduction in effective coupling strength of electrodes near the end of a transducer.

Another recent development was the introduction by Krimholtz [10] of the circuit[2] of Fig. 2 as a replacement for the Mason bulk-wave circuit. As originally set forth by Leedom *et al.* [11], the purpose of this new circuit was to decrease the complexity of circuit model computation by representing an *entire transducer* by the single circuit of Fig. 2. Although this circuit is valid for an acoustic source term which is an *arbitrary scalar function of the acoustic propagation coordinate* x, it was originally applied by assuming the same electric field distribution of the crossed-field bulk-wave model, thus emulating the crossed-field Mason-circuit model.

It has since been proposed by Bahr and Lee [12] that the circuit of Fig. 2 can be used to give a better description of surface-wave transducer performance, including overtone operation and the effects of metallization ratio, if some scalar acoustic source distribution appropriate for surface waves is used. Accordingly, they took the field distributions found by Engan [8] for an infinite array of single electrodes, and used as the source term the normal component of electric field at the substrate surface with an appropriate normalization. The results were in generally good agreement with experimental data for single-electrode transducers operated at the fundamental, third, and fifth harmonics for metallization ratios between 0.2 and 0.7.

The present work extends the above results so that the circuit model of Fig. 2 can be used to give an accurate three-port characterization of transducers with any number of electrodes, single, double, or in arbitrary polarity sequence, for fundamental frequency or higher harmonic operation.

II. ELECTRIC SOURCE TERM FOR ACOUSTIC WAVES

In order to use the circuit model of Fig. 2, it is necessary to find a suitable scalar function of the (vector) electric field to use as a source term for acoustic waves. We make

[2] Krimholtz's circuit actually consists of the portion of Fig. 2 marked electrode region.

two fundamental assumptions in finding the electric fields. First is the approximation that the electric fields under a given electrode depend only on the dimensions and polarities of that electrode and its nearest and next-nearest neighbors (*local environment*). Second, we assume that the electrode widths and spacings are either all identical or that they vary so slowly from electrode to electrode that all electrodes within the local environment have identical dimensions. Therefore a single metallization ratio and a sequence of polarities describes the local environment and determines the electric fields under a given electrode. Obviously there is a finite number of polarity combinations, with end electrodes and next-to-the-end electrodes being special cases. By solving a set of electrostatic boundary value problems containing all possible local environments, we can develop expressions for the electric fields under any one electrode in any environment.

Fig. 3 shows the geometry for finding the electric fields. The coordinate along the acoustic propagation direction is x, and that normal to the substrate surface is z. The electrodes are assumed to be infinitesimally thin perfect conductors. Each electrode is assigned a potential $\pm V$ and we may take $V = 1$ without loss of generality. The voltage applied across the transducer is then $\Delta V = 2$.

Because of the assumptions above, it suffices to find the electric fields for a finite array of electrodes all of whose metallization ratios are the same

$$\eta_i \equiv \frac{S_i}{L_i} = \eta \tag{2}$$

and whose spacings $L_i = L$ are also all equal. In this study we set up an array of twelve electrodes and solved (as described below) for the electric fields for different sets of polarities $V_i (i = 1,\cdots,12)$. Combinations of polarities $V_i (i = 1,\cdots,12)$ were selected so as to encompass all possible *independent* local environment polarity sequences (subsections of the 12-electrode array consisting of at most five electrodes).

Note that each local polarity sequence $\mathcal{S}$ has a corresponding sequence $-\mathcal{S}$ where all polarities are reversed and also a sequence $\tilde{\mathcal{S}}$ which is $\mathcal{S}$ inverted with respect to x. Only the sequence $\mathcal{S}$ need be analyzed in the electrostatic boundary problem in order to also determine by symmetry the fields for sequences $-\mathcal{S}$, $\tilde{\mathcal{S}}$, and $-\tilde{\mathcal{S}}$. Consequently, it is found by inspection that there are 22 independent local polarity sequences $\mathcal{S}_p$, $(p = 1,\cdots,22)$ for the next-nearest-neighbor local environment approximation, including end electrodes and next-to-the-end electrodes as special cases. By analyzing each sequence for several values of the metallization ratio η we can use a

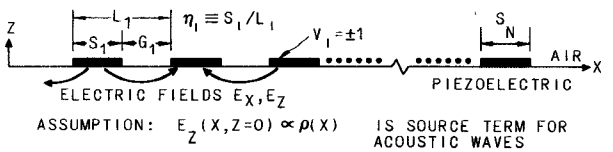

Fig. 3. Geometry for finding excitation electric fields in an interdigital transducer.

two-dimensional least squares fit against x and η to write the electric fields for one electrode $E_k(x,\eta)$ using well-known functions of x and η.

In view of the success of Bahr and Lee [12], we will use the normal electric field component $E_z(x,z = 0)$ appropriately normalized, as the scalar source term for the circuit model. For our infinitesimally thin electrodes, this field is zero in the gap regions and is proportional to the surface charge density $\rho(x)$ in the electrode regions. The boundary value problem for $\rho(x)$ is specified by the integral equation

$$V(x,0) = c_0 \int_{\text{array}} \log [(x - x')^2] \rho(x')\, dx' \tag{3}$$

with zero total charge condition

$$0 = Q = \int_{\text{array}} \rho(x)\, dx \tag{4}$$

and with potentials

$$V_i = \pm 1 \tag{5}$$

specified on the electrodes.

This boundary value problem was solved numerically for $\rho(x)$ by subdividing electrode i into small segments centered at the discrete points $x = x_{ik}$, each bearing charge $\rho_{ik} \equiv \rho(x_{ik})$, and converting (3)–(5) to a system of linear equations for ρ_{ik}. Further details of the solution of (3)–(5) are given in Appendix I and we note that this is essentially the same electrostatic boundary value problem considered by Hartmann and Secrest [9]. Having found $E_z(x,z = 0) \propto \rho(x)$ for various values of η and V_i, we now write for the ith electrode

$$\frac{E_z(x_i,\eta_i)\,|_{z=0}}{(\Delta V/L_i)} = -\frac{AL_i}{2} \sum_{m=0}^{\mathfrak{M}-1} (\eta_i - 0.5)^m \sum_{n=0}^{\mathfrak{N}-1} \alpha_{nm}^{(pi)} \cdot \frac{T_n(2x_i/\eta_i L_i)}{[(\eta_i L_i/2)^2 - x_i^2]^{1/2}}. \tag{6}$$

Here T_n is the Chebyshev polynomial of order n and the coefficients $\alpha_{nm}^{(pi)}$ are found by least squares fit of the charge density $\rho(x)$ against $\eta (0 < \eta < 1)$ and the continuous variable x_i in the region of the ith electrode. In this study $\mathfrak{N},\mathfrak{M} = 6$ were used. The parameter A is a dielectric constant ratio given by

$$A = 2\pi[\epsilon_{xx}/\epsilon_{zz} - \epsilon_{xz}^2/\epsilon_{zz}^2]^{1/2}. \tag{7}$$

This anisotropy factor relates the field

$$E_z(x_i,\eta_i)\,|_{z=0}/(\Delta V/L_i)$$

to the double sum on the right-hand side of (6), which is also proportional to $\rho(x)$.

Note that the expression (6) is to be used for any electrode i in any transducer where the local metallization ratio has the value η_i and the local polarity sequence around electrode i is $\mathcal{S}_p$. Appendix II tabulates the 22 independent sets of coefficients $\alpha_{nm}^{(p)}$ corresponding to

the 22 independent sequences $\mathcal{S}_p$. Note that $-\alpha_{nm}{}^{(p)}$ corresponds to sequence $-\mathcal{S}_p$, and $(-1)^m\alpha_{nm}{}^{(p)}$ corresponds to sequence $\tilde{\mathcal{S}}_p$, and $(-1)^{m+1}\alpha_{nm}{}^{(p)}$ corresponds to sequence $-\tilde{\mathcal{S}}_p$, because of the parity of the Chebyshev polynomials. The α coefficients were extracted from numerical charge density solutions in an array of 12 electrodes. Each sequence $\mathcal{S}_p$ listed in Appendix II consists of, at most, five contiguous electrodes (extracted from the 12-electrode array) because we apply the results under the approximation that only the nearest and next-nearest electrodes influence the charge on any given electrode. The coefficients in Cases 1–12 of Appendix II were obtained from the charge density on the end and next-to-the-end electrodes of the array, while those for interior electrodes (Cases 13–22) were obtained from the charge density on electrodes near the center of the array. No significant differences were found when the charge density calculations were repeated using a *20*-electrode array. We conclude that the 12-electrode array was sufficiently large that the interior electrodes were not influenced by end effects.

III. USE OF ELECTRIC FIELDS IN EQUIVALENT CIRCUIT MODEL

In the equivalent circuit of Fig. 2, the parameter C is the capacitance associated with the charge and voltage on one electrode. Integrating the charge density distribution [double sum in (6)] from $x_i = -\eta_i L_i/2$ to $x_i = \eta_i L_i/2$ results in a contribution to the total charge from the $n = 0$ terms only, yielding

$$C = C_i = \frac{Q_i}{(\Delta V)} = \frac{\pi A}{2}\epsilon_{zz}\sum_{m=0}^{\mathfrak{M}-1}\alpha_{0m}{}^{(p_i)}(\eta_i - 1/2)^m. \quad (8)$$

The parameters Y_S and Y_G in Fig. 2 are the acoustic-wave admittances, while Ψ and φ are the acoustic transit angles of the electrode and gap regions, respectively. The transit angles are given by

$$\Psi = \omega S/v_S \quad (9)$$

and

$$\varphi = \omega G/v_G \quad (10)$$

where ω is the angular frequency, S and G the respective widths of the electrode and gap, with v_S and v_G taken as the corresponding acoustic velocities.

In this study we use the circuit of Fig. 2 for one electrode and the adjacent gap only, and cascade the individual electrode circuits in the usual way [1], [3] to represent the entire transducer. In this way, the acoustic reflections due to the different acoustic-wave admittances of electrodes and gaps ($Y_S \neq Y_G$) can be properly described. When $Y_S = Y_G$, the electrode-region portion of Fig. 2 can be used to represent an *entire* transducer.[3] Also, provided that Y_S and Y_G are *nearly* equal and the number of electrodes is not too large, that single circuit is a good approximation for an entire transducer if the transmission lines (Y_S,Ψ) are replaced by a sequence of lines of alternating admittances Y_S and Y_G corresponding to the electrodes and gaps of the entire transducer [13]. Nevertheless, we eliminate that approximation here by using the cascade procedure and one circuit for each electrode.

As explained in [10]–[12], the parameter r of the equivalent circuit of Fig. 2 is given by

$$r = j\beta Y_S{}^{-1/2}F_0(\beta). \quad (11)$$

The J-inverter has the property of acting like a quarter-wave transmission line at all frequencies. Its $ABCD$ matrix is

$$\begin{bmatrix} 0 & j/B_2 \\ jB_2 & 0 \end{bmatrix}$$

where

$$B_2 = -\beta F_e(\beta)\, Y_S{}^{1/2}. \quad (12)$$

In (11) and (12) β is the wavenumber, and $F_e(\beta)$ and $F_0(\beta)$ are the real and imaginary parts of the (spectral) excitation function, which we choose as

$$F(\beta) \rightarrow F_i(\beta,\eta_i) = \left[\frac{4}{\pi}\frac{\beta_0}{\beta}\cdot f_i k_0{}^2 C_i \Big|_{\eta_i=1/2}\right]^{1/2} \cdot \mathfrak{F}\left\{\left(\frac{2\pi}{A}\right)\frac{E_z(x_i,\eta_i)\,|_{z=0}}{(\Delta V/L_i)}\right\} \quad (13)$$

where $\mathfrak{F}$ denotes the Fourier transform with argument β. This choice corresponds to using as the excitation function an appropriately normalized version of the E_z component under the ith electrode. The wavenumber β_0 is a reference wavenumber, usually at the center of the fundamental transducer response, while f_i is the half-wavelength frequency of the ith electrode. The substrate coupling constant $k_0{}^2$ may be taken as $2\Delta v/v$ where $\Delta v/v$ is the fractional velocity change calculated by Campbell and Jones [14]. The factor in square brackets is a normalizing factor closely related to the transformer ratio of the ordinary Mason bulk-wave circuit as applied with surface-wave parameters [1]–[3]. The factor (β_0/β) in the square bracket represents a filling factor resulting from the fact that the electric field penetration depth is determined by the transducer geometry or fundamental wavenumber β_0, while the penetration depth of surface elastic waves varies inversely with frequency [12]. This choice agrees with the normal mode theory of Auld and Kino [15].

In [12] the factor $(2\pi/A)$ was inadvertently omitted [16] in the published expression for the excitation function although it was actually included in the work. Its inclusion is necessary for agreement with [15] as well as with experiment on highly anisotropic substrates such as YZ lithium niobate where $2\pi/A \cong 0.4$ as compared to unity for a dielectrically isotropic material. Its inclusion corresponds to using as the source term the normal or z component of electric field but renormalizing its magnitude to equal the magnitude of the parallel component E_x. This is plausible because $k_0{}^2 = 2\Delta v/v$ is associated with the slowing of surface waves by shorting out E_x rather than E_z.

[3] A condition that is nearly realized under appropriate combination of the following conditions: double electrodes, few electrodes, or a weak-coupling substrate such as quartz.

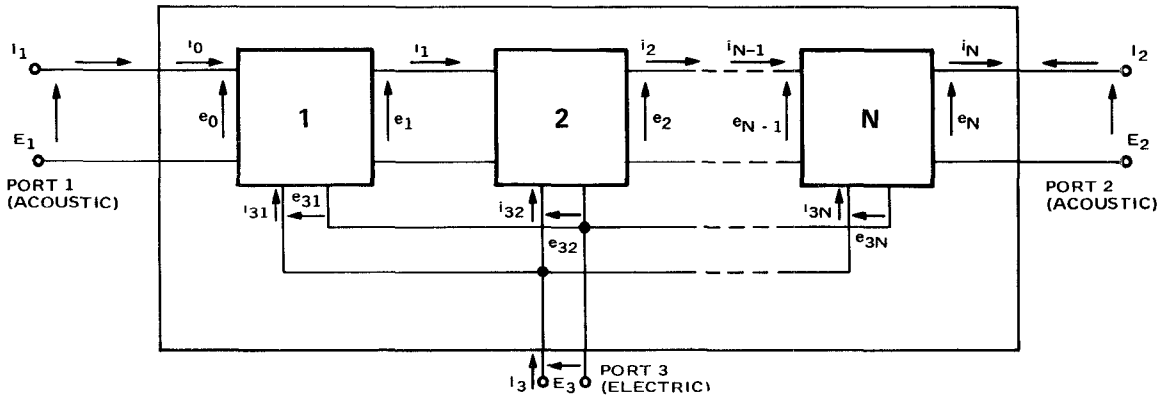

Fig. 4. Transducer composed of N sections, acoustically in cascade and electrically in parallel.

The shunt element jB_1 is given by

$$B_1 = \tfrac{1}{2}\mathcal{H}(|\beta F(\beta)|^2) \tag{14}$$

where $\mathcal{H}$ denotes the Hilbert transform. This element is necessary so that the network of Fig. 2 is a causal circuit. Evaluation of this transform will be discussed in Section IV. The admittance coefficients for the circuit of Fig. 2 are given in Appendix II.

Performing the Fourier transform indicated in (13) yields

$$F_i(\beta,\eta_i) = \left[\frac{4}{\pi}\frac{\beta_0}{\beta} f_i k_0^2 C_i \Big|_{\eta_i=1/2}\right]^{1/2} \cdot \left(\frac{2\pi}{A}\right)\left(\frac{\beta L_i}{2}\right) \cdot \sum_{m=0}^{\mathfrak{N}-1} (\eta_i - 1/2)^m \sum_{n=0}^{\mathfrak{N}-1} \alpha_{nm}^{(pi)} (-j)^n J_n\left(\frac{\beta\eta_i L_i}{2}\right). \tag{15}$$

The reason for using Chebyshev polynomials in the electric field expansion is now apparent; the expansion for E_z transforms term by term into the cylindrical Bessel functions J_n given in (15). *Equation (15) is the key result of this paper since, with the α coefficients tabulated in Appendix II, it completes the circuit of Fig. 2 for any electrode in any environment.* In order to select the proper set of α's for a given electrode, one notes the polarities of the nearest and next-nearest neighbors, invokes any necessary symmetry rules as described above, and refers to the case numbers listed in Appendix II. Our circuit model computer program includes such an algorithm for selecting the proper α's for each electrode. The program then cascades the circuits of the various electrodes to form the circuit for the entire transducer and finds all the three-port transfer functions. It can also analyze delay lines or filters with two transducers and systems with two sequential filters. Each transducer may be periodic or dispersive, apodized[4] or unapodized, with arbitrary polarity sequences, but the electrode dimensions must not vary too rapidly from electrode to electrode.

[4] When the transducer is apodized and operated in a filter whose other transducer is unapodized, the expression for $F_i(\beta,\eta_i)$ given in (13) and (15) must be multiplied by $(w_i/w_0)^{1/2}$. Here w_i is the aperture of the ith electrode and w_0 is the largest aperture of any electrode in the apodized transducer.

IV. NETWORK ANALYSIS FOR THE ENTIRE TRANSDUCER

The network for the entire transducer consisting of N electrodes is obtained by interconnecting the individual electrode networks (Fig. 2) according to the block diagram of Fig. 4. It is convenient to describe each individual network in terms of admittance coefficients y_{ij} which are easily found by circuit analysis of Fig. 2 and given in Appendix III. The recursion relations for combining the y_{ij} of all electrodes to find the Y_{ij} admittance coefficients of the entire transducer are given in [3, appendix A]. The Y_{ij} coefficients of the transducer are of course sufficient to characterize all its three-port transfer properties by the analysis described (for example) in [1] and [3].

All the elements in the one-electrode network (Fig. 2) were specified in Section III. The element jB_1 requires evaluation of a Hilbert transform of $|\beta F(\beta)/2|^2$ which must be done by numerical methods. It is clearly disadvantageous to calculate and store $|\beta F(\beta)/2|^2$ as a function of frequency for all N electrodes and then to perform N numerical Hilbert transforms to find the N separate elements jB_1 for the N electrodes. It is shown in Appendix III that the correct Y_{ij} coefficients of the entire transducer can be obtained even if the elements jB_1 are omitted for each electrode. After all of the one-electrode circuits are cascaded according to the block diagram of Fig. 4, a single Hilbert transform can be used to find a single added susceptive element across the transducer's electrical port, yielding the same result that would have been found if all the jB_1 elements had not been omitted.

V. ILLUSTRATIVE RESULTS

A. Coupling for Single Electrodes with Arbitrary Metallization Ratios up to the Eleventh Harmonic

The first case investigated with the new circuit model is a periodic, single-electrode transducer with 20 electrodes. This is an excellent approximation to an infinite transducer and provides a test case since the infinite periodic transducer was analyzed in [12] with the same circuit model and the fields from [8]. A convenient

measure of the coupling is the effective k^2 defined by

$$k_{\text{eff}}^2 = \frac{\pi Q_r^{-1}}{2N} \tag{16}$$

where N is the number of electrodes in the transducer and Q_r is the radiation Q, given by

$$Q_r = \frac{2\pi f_M C_T}{G_a(f_M)} \tag{17}$$

i.e., the ratio of capacitive susceptance to the radiation conductance at the Mth harmonic frequency f_M. The effective k^2 is proportional to the intrinsic substrate coupling $k_0^2 = 2\Delta v/v$. Therefore, in Fig. 5 we plot k_{eff}^2/k_0^2 versus metallization ratio η for the harmonics M = 1,3,5, 7,9,11, for 20 (many) single electrodes. These curves are in agreement with the formula given in [12], where experimental points from various authors were also found to agree reasonably well with the theory for M = 1,3,5. We reemphasize that the effective k^2 at the harmonic frequencies is only one representative result from the circuit model which can calculate all the transducer three-port properties at all frequencies [1], [3]. One point is provided in Fig. 5 to illustrate end effects in short transducers. The effective k^2 for a 5-electrode transducer with η = 0.5 operating at the fundamental frequency is shown by the large dot labeled 5 electrodes. There is an 8-percent reduction in k_{eff}^2 caused by end effects in the 5-electrode transducer. The shape of the insertion loss function (not shown) also deviates somewhat from the usual $(\sin x/x)^2$ shape because of end effects.

B. Coupling for Double Electrodes with Arbitrary Metallization Ratios up to the Eleventh Harmonic

Fig. 6 shows for double electrodes the effective k^2 curves which are analogous to those given in Fig. 5 for single electrodes. The curves were calculated for a 20-electrode transducer, which is again a good approximation to an infinite transducer. Note that the effective k^2 is the same for M = 1 and 3, for M = 5 and 7, and for M = 9 and 11. A similar result (coalescence) was found for the quantity $|\beta F(\beta)|$ for an infinite array of double electrodes in [9]. Again, the reduction in k_{eff}^2 caused by end effects on a 5-electrode transducer with η = 0.5 is indicated by the heavy dot for M = 1 (fundamental) and for M = 3.

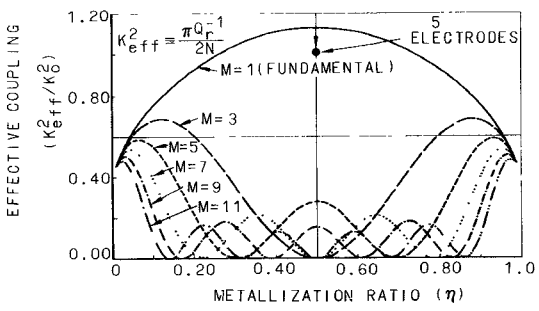

Fig. 5. Effective coupling versus metallization ratio for a periodic transducer with many ($\geq$ 20) single electrodes.

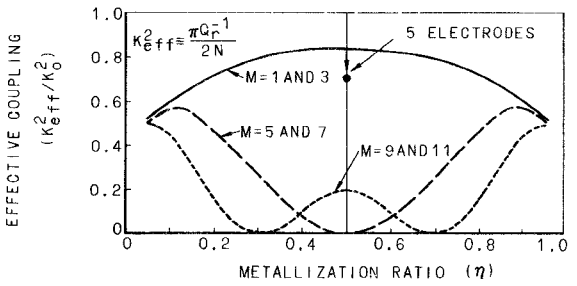

Fig. 6. Effective coupling versus metallization ratio for a periodic transducer with many ($\geq$ 20) double electrodes.

C. Theoretical and Experimental Results for an Efficient Ninth-Harmonic Transducer

Two devices having transducers of 10 double electrodes were designed, fabricated, and tested with two goals: 1) to verify the curves in Fig. 6, and 2) to achieve efficient operation at a high harmonic (in this case the ninth harmonic). According to the data of Fig. 6, the effective k^2 for the ninth and eleventh harmonics has a relative maximum for η = 0.5 and absolute maxima near η = 0.1 and 0.9. Consequently, two devices were designed with planned metallization ratios η = 0.5 and η = 0.9. In the actual devices, measured values of η were 0.56 $\pm$ 0.05 and 0.88 $\pm$ 0.05. Theoretical curves for the insertion loss of each delay line were calculated and it was found that η = 0.58 and η = 0.90 give best agreement with the measured results.

Fig. 7(a) shows the calculated insertion loss function for the η = 0.58 delay line. Note that the insertion loss itself is not $-20 \log_{10} k_{\text{eff}}^2$, but depends on the impedance match between transducer and source at all frequencies. Hence, the insertion loss for the untuned transducer is

$$IL = -20 \log_{10} \frac{2G_L G_a(f)}{(G_L + G_a(f))^2 + (2\pi f C_T)^2} \tag{18}$$

i.e., it is dependent on the radiation conductance $G_a(f)$, which is proportional to k_{eff}^2, and it is also dependent on the capacitive susceptance $2\pi f C_T$ and the source conductance G_L. The transducer aperture was chosen so that $2\pi f C_T \cong G_L$ near the ninth harmonic, a design that minimizes the ninth-harmonic insertion loss at the expense of higher insertion loss at other harmonics.

The measured insertion loss for this device is shown in Fig. 7(b). The agreement between theory and experiment is generally excellent with all harmonic insertion losses agreeing within 2 dB or better, and all sidelobes at approximately the correct level with the proper sense of tilt (up or down) between the nearest sidelobes at each harmonic. The fact that the metallization ratio is somewhat larger than intended (η = 0.58 instead of 0.50) results in the presence of fifth and seventh harmonic response. They are still about 10 dB below the ninth harmonic, but their presence and level are probably the most sensitive measure of the metallization ratio as might be expected from Fig. 6. The fact that the metallization ratio is 0.58 instead of 0.50 also makes the ninth and eleventh harmonics less efficient than planned.

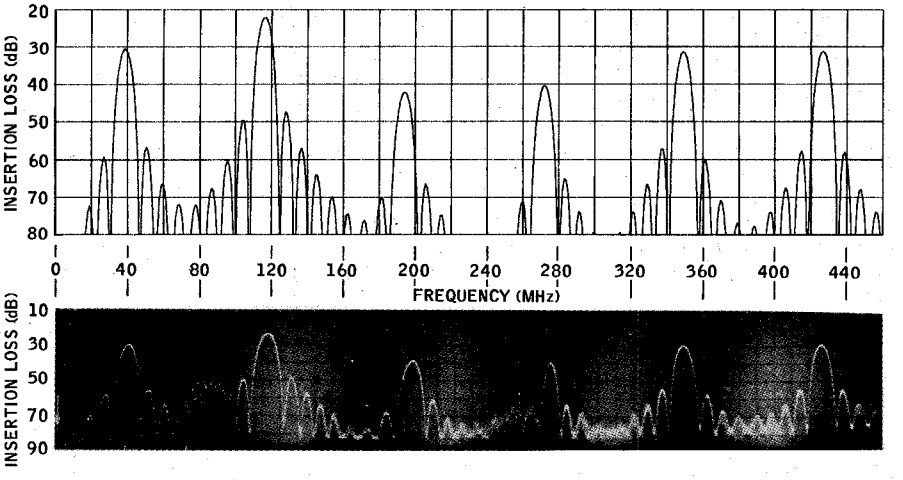

Fig. 7. Theoretical and experimental insertion loss of a delay line with 10-double-electrode transducers on *YZ* lithium niobate. Theoretical metallization ratio $\eta = 0.58$; experimental metallization ratio $\eta = 0.56 \pm 0.05$. (a) Theory. (b) Experiment.

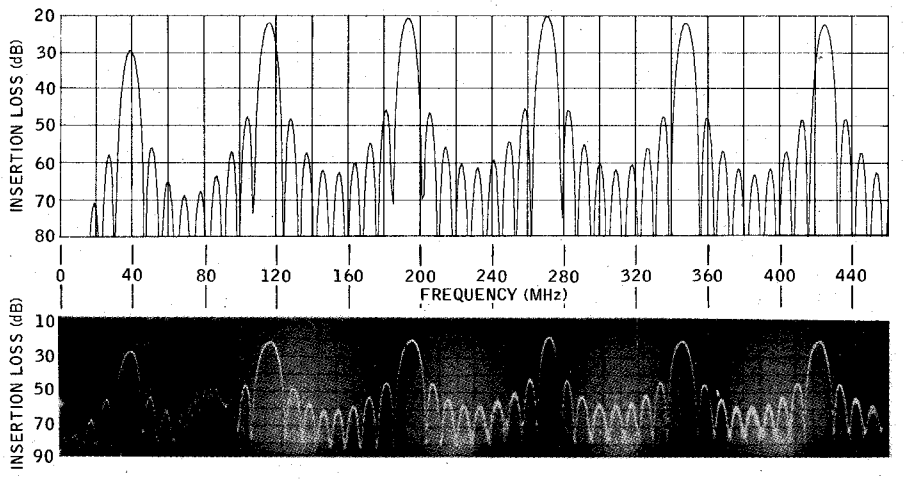

Fig. 8. Theoretical and experimental insertion loss of a delay line with 10-double-electrode transducers on *YZ* lithium niobate. Theoretical metallization ratio $\eta = 0.90$; experimental metallization ratio $\eta = 0.88 \pm 0.05$. (a) Theory. (b) Experiment.

The experimental curve in Fig. 7(b) consists of five Polaroid photos placed contiguously; the left-hand panel covers approximately 0–90 MHz and was taken with the Hewlett-Packard low-frequency network analyzer while the remaining four panels were taken with the high-frequency network analyzer.

Aside from the fact that the theory does not account for bulk waves (note bulk-wave response near 80 and 250 MHz), the agreement between theory and experiment is excellent. Most important is the correct prediction of relative harmonic levels, which is most significant for overtone operation. This capability is totally absent from the ordinary crossed-field bulk-wave model.

Agreement between theory and experiment is even better for the 90-percent-metallization-ratio transducers, as evidenced by the data of Fig. 8. The effective k^2, from Fig. 6, is roughly equal for the first eleven harmonics near $\eta = 0.9$, and the ninth harmonic k^2 is more than 3 times higher at $\eta = 0.9$ than at $\eta = 0.58$. Consequently, this device has about 10 dB less insertion loss at the ninth harmonic than the $\eta = 0.58$ device. Although fabrication of transducers with $\eta = 0.9$ is difficult at higher frequencies, the data of Figs. 7 and 8 confirm the accuracy of the new circuit model. Furthermore, we have achieved efficient operation at the ninth and eleventh harmonics. By tuning and matching at the ninth harmonic, the insertion loss can theoretically be reduced to the 6-dB bidirectional loss. The most important property, however, is the insertion-loss/bandwidth tradeoff [5, eq. (32)] fixed by the effective k^2 given in Fig. 6. For double electrodes at $\eta = 0.9$, the effective k^2 is slightly less than half the intrinsic substrate k^2, i.e., $k_0^2 = 2\Delta v/v$.

D. Theoretical and Experimental Results for a Phase-Reversal Transducer

An example of a device with a nonalternating polarity sequence is a 13-electrode PRT [17] where the last two electrodes on each end are reversed in polarity with respect to the normal alternating sequence in the central 9 electrodes. We have fabricated two delay lines using 13-electrode PRT's on *YZ* lithium niobate with a fundamental frequency of 30 MHz. The first such delay line has single

electrodes with $\eta = 0.5$ and its theoretical and experimental insertion loss functions are compared in Fig. 9. The solid curve labeled new theory was calculated from the present analysis while the old theory (dashed curve) refers to the ordinary crossed-field Mason-circuit model. The new theory correctly explains the following features not found in the ordinary crossed-field model predictions: 1) absence of a third harmonic response, 2) roll-up of about 2 dB in the main passband, and 3) relatively high level of the first sidelobes.

The same comparison is made for a PRT with 13 *double* electrodes in Fig. 10. The new theory is superior in much the same way as for single electrodes. First, it correctly predicts a strong third-harmonic response: the insertion loss is slightly lower at the third harmonic than at the fundamental, while the ordinary crossed-field model predicts the opposite. Second, it correctly predicts a roll up in both the fundamental and third-harmonic passbands, although somewhat less accurately at the third harmonic than at the fundamental. Third, the new theory gives a good prediction of the nearest sidelobe levels while the ordinary crossed-field model does not.

VI. SUMMARY OF NEW CIRCUIT MODEL RESULTS

The circuit model proposed in [10]–[12] is now reduced to routine practice since the indicated electric driving functions have been found here and the design engineer no longer needs to solve the electrostatic boundary problem for his particular transducer. The circuit model appears successful in handling end effects, harmonic operation, and arbitrary electrode polarity sequences as was to be expected from using a good approximation to the electric fields under an interdigital transducer.

Accurate description of end effects is important because many devices employ short broad-band transducers in tapped delay lines or as input transducers to drive a long dispersive or coded transducer. The PRT is a widely used transducer for flat passbands, and the circuit model, which accurately modeled the polarity reversals of PRT's, is probably equally accurate for coded (e.g., Barker) transducers. Furthermore, the results can easily be extended to model broken electrodes by redoing the electrostatic boundary value problems to include cases with a stripe floating at some intermediate voltage. On the other hand, the *synthesis* procedure which was developed in [3] for the ordinary crossed-field model has not yet been updated to include the effects described by the new circuit model.

The effective k^2 results given here were calculated without the use of different acoustic-wave impedances for the electrode and gap regions. However, the discontinuity parameter $Y_S/Y_G = 1.018$ was used in the PRT analysis, an especially important choice for the single-electrode PRT.

The new model also exhibits the crossed-field-model property whereby low impedance loads minimize acoustic

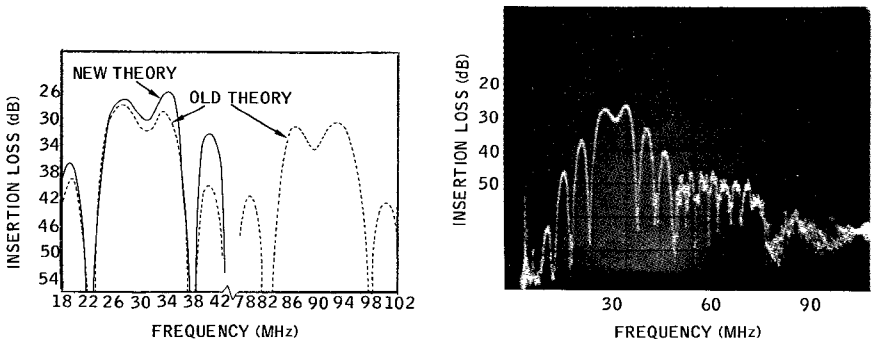

Fig. 9. Theoretical and experimental insertion loss of a delay line with PRT's having 13 single electrodes. (a) Theory—solid curve, new circuit model; dashed curve, ordinary crossed-field model. (b) Experiment.

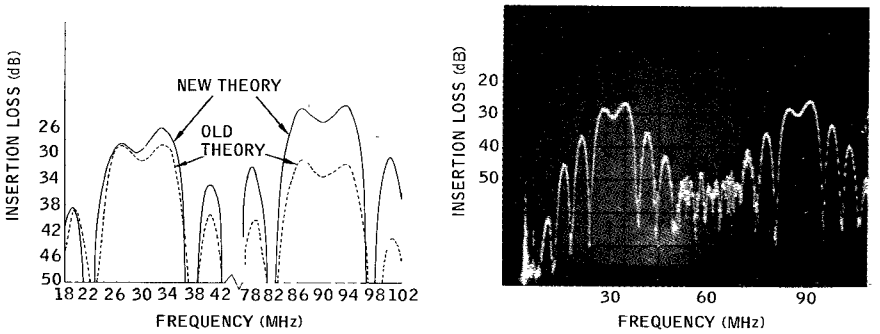

Fig. 10. Theoretical and experimental insertion loss of a delay line with PRT's having 13 double electrodes. (a) Theory—solid curve, new circuit model; dashed curve, ordinary crossed-field model. (b) Experiment.

regeneration from the load, as previously verified experimentally [18].

The new circuit model retains the procedure of cascading individual electrode circuits to avoid approximations about the spatial distribution of driving fields among the electrodes and gaps of alternating acoustic-wave admittance. When increased computational efficiency is essential, one can adopt the philosophy of [13], where one lumped circuit is used for the electroacoustic generation of surface waves, and the alternating wave admittances of electrodes and gaps are modeled by external transmission lines. In order to do this, the appropriate driving function $F(\beta)$ should be taken as

$$F(\beta) = \sum_i F_i(\beta,\eta_i) \exp(-j\beta x_i). \tag{19}$$

The accuracy of adopting this procedure decreases as the number of electrodes, the substrate k_0^2, and the electrode mass loading increase.

The computer program associated with the new circuit model is completed for all types of nonperiodic apodized transducers and for combining the transducers into filters and transmit/receive loops as might be used in radar and communication systems. However, it has not yet actually been applied to any transducers other than those described in this paper and it is recommended that the analysis be used also for dispersive and/or apodized transducers as requirements dictate. One further modification to the circuit model could improve its accuracy in describing acoustic reflections, namely, the addition of shunt susceptive elements on the acoustic ports to represent energy storage at the edges of the electrodes [19].

APPENDIX I

SOLUTION FOR NORMAL ELECTRIC FIELD IN A FINITE ARRAY OF THIN ELECTRODES ON THE SURFACE OF A DIELECTRIC SUBSTRATE

The electrostatic boundary value problem for finding the normal electric field in an interdigital transducer is posed under the assumption that the fields under one electrode depend only on the geometry and polarity of near-neighbor electrodes. It is also assumed that the electrodes are infinitesimally thin and that the electrode spacings and widths vary slowly or not at all throughout the transducer. Pursuant to these assumptions, it is sufficient to find the normal electric field in a finite array of electrodes which are uniformly spaced. The electrode-width-to-spacing (metallization) ratio is a variable, albeit the same for all electrodes. Thus the electrodes are identical except that the polarities (+ or −) may be specified in arbitrary sequence. By using an array of J electrodes spaced by a distance L, and solving the boundary value problem for various polarity sequences, we can find expressions for the normal electric field at the surface for end and interior electrodes, single and double electrodes, and electrodes having nonalternating polarity sequences. The geometry for the electrostatic boundary value problem solution is shown in Fig. 11.

The normal electric field at the surface $E_z(x,z=0)$, is proportional to the surface charge density $\rho(x)$ on the electrode; there is no normal field in the gaps for infinitesimally thin electrodes. We must therefore solve the integral equation

$$V(x,0) = c_0 \int_0^{JL} \log[(x-x')^2]\rho(x')\,dx' \tag{20}$$

over the array having J elements of length L.

The constant c_0 is given by

$$c_0 = \frac{1}{2\pi\{[\epsilon_{xx}\epsilon_{zz} - \epsilon_{xz}^2]^{1/2} + \epsilon_0\}} \tag{21}$$

where $\epsilon_{xx},\epsilon_{zz},\epsilon_{xz}$ are substrate dielectric permittivities, and ϵ_0 is the permittivity of free space.

The boundary conditions are

$$V(x,0) = V_0 + V_i \quad \text{for} \quad |x - x_{ic}| \le \frac{S}{2} \tag{22}$$

where x_{ic} is the center of the ith electrode, and the condition of zero total charge is

$$0 = \int_0^{JL} \rho(x)\,dx. \tag{23}$$

These integral equations can be reduced to a set of linear algebraic equations via the following steps, where singly subscripted x variables are continuous, and multiply subscripted x's are discrete:

1) subdividing each electrode into $\mathfrak{N}$ equal segments and discretizing x in (20) to the values x_{ik} (i = electrode number, k = segment number);
2) defining the center of electrode j as x_{jc};
3) substituting the following form for $\rho(x_j')$ in the region of electrode j:

$$\rho(x_j') = \sum_{n=0}^{\mathfrak{N}-1} \frac{\gamma_{jn} T_n(2x_j'/S)}{[(S/2)^2 - x_j'^2]^{1/2}} \tag{24}$$

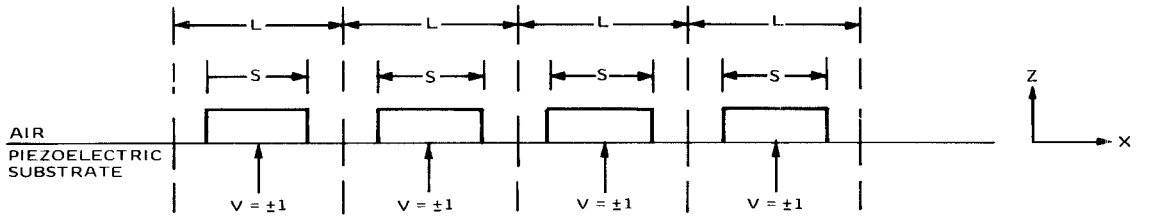

Fig. 11. Geometry for finding normal electric field at surface under electrodes.

where $x_j' = x' - x_{jc}$, T_n is the Chebyshev polynomial of order n, and the γ_{jn} are coefficients to be determined;

4) also, defining $x_{ikj} = x_{ik} - x_{jc}$. Thus (20)–(23) are reduced to the following set of $(\mathfrak{N}J) + 1$ linear algebraic equations for the γ_{jn} and for V_0:

$$\pm 1 = V_{ik} = 2c_0 \sum_{j=1}^{J} \sum_{n=0}^{\mathfrak{N}-1} \left\{ \int_{-S/2}^{S/2} \frac{T_n(2x'/S) \log \mid x_{ikj} - x_j' \mid dx_j'}{[(S/2)^2 - x_j'^2]^{1/2}} \right\} \gamma_{jn} - V_0$$

$$0 = \sum_{j=1}^{J} \sum_{n=0}^{\mathfrak{N}-1} \left\{ \int_{-S/2}^{S/2} \frac{T_n(2x_j'/S)\, dx_j'}{[(S/2)^2 - x_j'^2]^{1/2}} \gamma_{jn} \right\}. \tag{25}$$

By repeating the solution of these equations for various sets of $(V_i, i = 1, \cdots, 12)$ and values of $\eta = S/L$, $0 < \eta < 1$, we can use a least squares fit to express γ_{jn} as

$$\gamma_{jn} = \sum_{m=0}^{\mathfrak{N}-1} \alpha_{nm}{}^{j} (\eta - 0.5)^m. \tag{26}$$

Thus we arrive at the following form for $E_z(x,z=0) \propto \rho(x)$ which we normalize to $(\Delta V/L)$:

$$\frac{E_z(x_j,\eta) \mid_{z=0}}{(\Delta V/L)} = -\frac{AL}{2} \sum_{m=0}^{\mathfrak{N}-1} (\eta - 0.5)^m \cdot \sum_{n=0}^{\mathfrak{N}-1} \alpha_{nm}{}^{j} \frac{T_n(2x_j/\eta L)}{[(\eta L/2)^2 - x_j^2]^{1/2}} \tag{27}$$

where the subscript j on the continuous variable x_j indicates that this expression represents the fields under one electrode. The constant A is that given in Section II. The $\alpha_{nm}{}^{j}$ depend on near-neighbor-electrode polarities and are tabulated for the various possible neighbor-polarity combinations in Appendix II.

APPENDIX II

CATALOG OF ALPHAS FOR SPECIFYING NORMAL ELECTRIC FIELD UNDER AN ELECTRODE, GIVEN NEAR-NEIGHBOR POLARITIES

This Appendix gives the 22 independent sets of α's for finding the normal electric field under one electrode according to the expression

$$\frac{E_z(x_i,\eta_i) \mid_{z=0}}{\Delta V/L_i} = \frac{-AL_i}{2} \sum_{m=0}^{\mathfrak{N}-1} (\eta_i - \tfrac{1}{2})^m \cdot \sum_{n=0}^{\mathfrak{N}-1} \alpha_{nm}{}^{(pi)} \cdot \frac{T_n(2x_i/\eta_i L_i)}{[(\eta_i L_i/2)^2 - x_i^2]^{1/2}}.$$

The 22 cases are listed by showing the local environment polarity sequence $\mathcal{S}_p$ for case number p. As described in the text, $-\alpha_{nm}{}^{(p)}$ is associated with $-\mathcal{S}_p$, $(-1)^n \alpha_{nm}{}^{(p)}$ is associated with $\tilde{\mathcal{S}}_p$, and $(-1)^{n+1}\alpha_{nm}{}^{(p)}$ with $-\tilde{\mathcal{S}}_p$. The encircles polarity sign refers to the electrode under which the above expression applies.

Interactions from *nearest* neighbor electrodes only are described by the following 5 independent sets of α's:

Case 1N left-end electrode $\oplus$ $-$, same α_{nm} as Case 2;
Case 2N left-end electrode $\oplus$ $+$, same α_{nm} as Case 3;
Case 3N interior electrode $-$ $\oplus$ $-$, same α_{nm} as Case 20;
Case 4N interior electrode $+$ $\oplus$ $-$, same α_{nm} as Case 17;
Case 5N interior electrode $+$ $\oplus$ $+$, same α_{nm} as Case 18.

CASE 1 LEFT END ELECTRODE ⊕ - -

NJ M-> 0	1	2	3	4	5
01 8.011E-02	8.908E-02	4.159E-02	1.023E-01	1.489E-01	3.814E-01
11 2.214E-02	7.722E-02	9.877E-02	1.335E-01	3.453E-01	5.736E-01
21 3.047E-03	1.645E-02	4.479E-02	8.007E-02	2.376E-01	4.239E-01
31 4.370E-04	3.794E-03	1.291E-02	3.382E-02	1.384E-01	2.699E-01
41 6.462E-05	7.095E-04	2.753E-03	9.969E-03	5.618E-02	1.173E-01
51 1.078E-05	1.354E-04	4.165E-04	2.436E-03	2.312E-02	5.319E-02

CASE 2 LEFT END ELECTRODE ⊕ - +

NJ M-> 0	1	2	3	4	5
01 7.213E-02	8.513E-02	4.566E-02	9.883E-02	1.549E-01	3.701E-01
11 2.098E-02	7.671E-02	1.031E-01	1.349E-01	3.453E-01	5.729E-01
21 3.314E-03	2.019E-02	4.878E-02	8.399E-02	2.400E-01	4.254E-01
31 5.132E-04	4.358E-03	1.479E-02	3.690E-02	1.421E-01	2.734E-01
41 7.781E-05	8.440E-04	3.283E-03	1.119E-02	5.830E-02	1.196E-01
51 1.284E-05	1.601E-04	5.396E-04	2.828E-03	2.420E-02	5.476E-02

CASE 3 LEFT END ELECTRODE ⊕ + -

NJ M-> 0	1	2	3	4	5
01 3.353E-02	1.234E-02	-8.836E-03	1.021E-02	-1.957E-02	3.305E-02
11 -4.253E-03	-1.253E-02	-9.036E-03	-2.441E-03	-3.459E-03	5.347E-05
21 -1.239E-03	-6.287E-03	-1.081E-02	-8.485E-03	-7.149E-03	-6.521E-03
31 -2.114E-04	-1.553E-03	-4.444E-03	-6.880E-03	-9.036E-03	-9.925E-03
41 -3.123E-05	-2.995E-04	-1.174E-03	-2.693E-03	-5.034E-03	-6.177E-03
51 -4.595E-06	-5.447E-05	-2.646E-04	-8.512E-04	-2.539E-03	-3.932E-03

CASE 4 LEFT END ELECTRODE ⊕ + +

NJ M-> 0	1	2	3	4	5
01 2.278E-02	7.440E-03	-3.860E-03	5.538E-03	-1.126E-02	1.807E-02
11 -5.452E-03	-1.287E-02	-3.562E-03	-1.145E-03	-2.819E-03	-5.300E-04
21 -8.393E-04	-3.862E-03	-5.652E-03	-3.746E-03	-4.074E-03	-4.051E-03
31 -1.106E-04	-7.709E-04	-2.077E-03	-3.101E-03	-4.438E-03	-4.362E-03
41 -1.456E-05	-1.358E-04	-5.195E-04	-1.188E-03	-2.403E-03	-3.168E-03
51 -2.052E-06	-2.403E-05	-1.146E-04	-3.747E-04	-1.198E-03	-1.949E-03

CASE 5 SECOND ELECTRODE FROM LEFT - ⊕ - -

NJ M-> 0	1	2	3	4	5
01 1.147E-01	1.530E-01	9.439E-02	1.900E-01	3.240E-01	7.182E-01
11 2.271E-04	-1.635E-04	-1.153E-03	2.906E-04	3.820E-04	5.046E-04
21 5.259E-03	3.246E-02	8.103E-02	1.509E-01	4.641E-01	8.359E-01
31 -2.278E-04	-1.478E-05	-1.708E-05	1.000E-04	4.581E-04	6.816E-04
41 1.155E-04	1.275E-03	4.876E-03	1.815E-02	1.074E-01	2.273E-01
51 -2.046E-07	-2.169E-06	-1.004E-05	-1.916E-05	1.911E-05	9.281E-05

CASE 6 SECOND ELECTRODE FROM LEFT - ⊕ - +

NJ M-> 0	1	2	3	4	5
01 1.070E-01	1.496E-01	9.846E-02	1.869E-01	3.297E-01	7.072E-01
11 -1.945E-03	-3.160E-03	2.309E-03	1.227E-03	-2.230E-04	-3.025E-04
21 5.763E-03	3.543E-02	8.714E-02	1.566E-01	4.682E-01	8.393E-01
31 5.369E-05	4.404E-04	1.428E-03	2.462E-03	3.070E-03	2.876E-03
41 1.331E-04	1.445E-03	5.581E-03	1.980E-02	1.106E-01	2.310E-01
51 1.418E-06	1.733E-05	8.746E-05	2.854E-04	8.965E-04	1.195E-03

CASE 7 SECOND ELECTRODE FROM LEFT - ⊕ + -

NJ M-> 0	1	2	3	4	5
01 6.981E-02	8.017E-02	4.365E-02	9.851E-02	1.554E-01	3.714E-01
11 -2.976E-02	-9.906E-02	-1.117E-01	-1.366E-01	-3.509E-01	-5.742E-01
21 1.582E-03	1.089E-02	3.109E-02	6.731E-02	2.246E-01	4.113E-01
31 -6.961E-04	-5.711E-03	-1.847E-02	-4.262E-02	-1.505E-01	-2.935E-01
41 3.262E-05	3.937E-04	1.466E-03	4.771E-03	4.921E-02	1.079E-01
51 -1.660E-05	-2.047E-04	-7.650E-04	-3.545E-03	-2.653E-02	-5.859E-02

CASE 8 SECOND ELECTRODE FROM LEFT - ⊕ + +

N| M->	0	1	2	3	4	5
0|	6.288E-02	7.816E-02	4.763E-02	9.537E-02	1.611E-01	3.603E-01
1|	-3.251E-02	-1.027E-01	-1.073E-01	-1.356E-01	-3.512E-01	-5.747E-01
2|	1.977E-03	1.326E-02	3.605E-02	7.188E-02	2.276E-01	4.138E-01
3|	-6.213E-04	-5.116E-03	-1.662E-02	-3.970E-02	-1.472E-01	-2.807E-01
4|	4.971E-05	5.604E-04	2.130E-03	8.289E-03	5.190E-02	1.109E-01
5|	-1.458E-05	-1.806E-04	-6.356E-04	-3.174E-03	-2.556E-02	-5.720E-02

CASE 9 SECOND ELECTRODE FROM LEFT + ⊕ - -

N| M->	0	1	2	3	4	5
0|	6.321E-02	7.439E-02	4.553E-02	9.598E-02	1.595E-01	3.633E-01
1|	3.234E-02	1.024E-01	1.072E-01	1.356E-01	3.516E-01	5.750E-01
2|	2.106E-03	1.392E-02	3.751E-02	7.424E-02	2.311E-01	4.171E-01
3|	6.287E-04	5.172E-03	1.680E-02	4.000E-02	1.478E-01	2.813E-01
4|	4.660E-05	5.368E-04	2.072E-03	8.333E-03	5.262E-02	1.124E-01
5|	1.469E-05	1.819E-04	6.417E-04	3.196E-03	2.566E-02	5.738E-02

CASE 10 SECOND ELECTRODE FROM LEFT + ⊕ - +

N| M->	0	1	2	3	4	5
0|	5.833E-02	7.149E-02	4.313E-02	9.357E-02	1.632E-01	3.557E-01
1|	3.075E-02	9.987E-02	1.097E-01	1.370E-01	3.503E-01	5.745E-01
2|	2.343E-03	1.557E-02	4.151E-02	7.840E-02	2.337E-01	4.189E-01
3|	6.622E-04	5.475E-03	1.786E-02	4.188E-02	1.498E-01	2.829E-01
4|	5.085E-05	6.607E-04	2.586E-03	9.549E-03	5.479E-02	1.148E-01
5|	1.596E-05	1.975E-04	7.209E-04	3.446E-03	2.629E-02	5.824E-02

CASE 11 SECOND ELECTRODE FROM LEFT + ⊕ + -

N| M->	0	1	2	3	4	5
0|	2.043E-02	2.523E-03	-5.848E-03	5.191E-03	-1.068E-02	1.925E-02
1|	2.434E-03	3.617E-03	-3.485E-03	-1.039E-03	2.165E-04	3.935E-04
2|	-1.772E-03	-8.693E-03	-1.423E-02	-1.081E-02	-9.752E-03	-8.897E-03
3|	-6.983E-05	-5.474E-04	-1.703E-03	-2.774E-03	-3.256E-03	-3.003E-03
4|	-4.008E-05	-3.809E-04	-1.485E-03	-3.390E-03	-6.470E-03	-8.080E-03
5|	-1.751E-06	-2.113E-05	-1.053E-04	-3.348E-04	-9.101E-04	-1.324E-03

CASE 12 SECOND ELECTRODE FROM LEFT + ⊕ + +

N| M->	0	1	2	3	4	5
0|	1.549E-02	1.584E-04	-2.529E-03	2.942E-03	-7.010E-03	1.139E-02
1|	4.414E-04	6.246E-04	-2.541E-04	1.496E-04	-7.791E-04	-2.257E-04
2|	-1.537E-03	-7.090E-03	-1.040E-02	-6.859E-03	-7.334E-03	-7.263E-03
3|	-2.045E-05	-1.410E-04	-3.720E-04	-5.464E-04	-8.272E-04	-1.056E-03
4|	-2.744E-05	-2.546E-04	-9.664E-04	-2.180E-03	-4.332E-03	-5.672E-03
5|	-2.284E-07	-2.485E-06	-1.266E-05	-4.444E-05	-1.684E-04	-2.955E-04

CASE 13 INTERIOR ELECTRODE - - ⊕ - -

N| M->	0	1	2	3	4	5
0|	1.130E-01	1.515E-01	9.380E-02	1.897E-01	3.249E-01	7.171E-01
1|	0.0	0.0	0.0	0.0	0.0	0.0
2|	5.470E-03	3.349E-02	8.273E-02	1.576E-01	4.664E-01	8.381E-01
3|	0.0	0.0	0.0	0.0	0.0	0.0
4|	1.178E-04	1.208E-03	4.975E-03	1.843E-02	1.084E-01	2.296E-01
5|	0.0	0.0	0.0	0.0	0.0	0.0

CASE 14 INTERIOR ELECTRODE - - ⊕ - +

N| M->	0	1	2	3	4	5
0|	1.099E-01	1.481E-01	9.460E-02	1.879E-01	3.275E-01	7.109E-01
1|	-3.047E-03	-3.587E-03	4.875E-03	6.301E-04	5.856E-05	-6.926E-04
2|	5.563E-03	3.449E-02	8.590E-02	1.565E-01	4.686E-01	8.395E-01
3|	8.642E-05	6.731E-04	2.032E-03	3.160E-03	3.515E-03	3.201E-03
4|	1.266E-04	1.390E-03	5.371E-03	1.941E-02	1.102E-01	2.306E-01
5|	2.190E-06	2.667E-05	1.283E-04	3.973E-04	1.042E-03	1.487E-03

CASE 15 INTERIOR ELECTRODE - - ⊕ + -

N| M->	0	1	2	3	4	5
0|	7.137E-02	7.876E-02	4.169E-02	9.954E-02	1.533E-01	3.750E-01
1|	-2.979E-02	-9.866E-02	-1.108E-01	-1.367E-01	-3.514E-01	-5.750E-01
2|	1.530E-03	1.060E-02	3.072E-02	6.771E-02	2.257E-01	4.123E-01
3|	-7.007E-04	-5.747E-03	-1.859E-02	-4.293E-02	-1.512E-01	-2.846E-01
4|	2.819E-05	3.542E-04	1.327E-03	6.550E-03	4.912E-02	1.080E-01
5|	-1.653E-05	-2.041E-04	-7.522E-04	-3.548E-03	-2.662E-02	-5.879E-02

CASE 16 INTERIOR ELECTRODE - - ⊕ + +

N| M->	0	1	2	3	4	5
0|	6.458E-02	7.674E-02	4.603E-02	9.623E-02	1.591E-01	3.639E-01
1|	-3.324E-02	-1.028E-01	-1.051E-01	-1.364E-01	-3.511E-01	-5.756E-01
2|	1.882E-03	1.208E-02	3.554E-02	7.217E-02	2.286E-01	4.146E-01
3|	-6.017E-04	-4.985E-03	-1.633E-02	-3.949E-02	-1.474E-01	-2.811E-01
4|	4.562E-05	5.244E-04	2.006E-03	8.089E-03	5.180E-02	1.110E-01
5|	-1.405E-05	-1.748E-04	-6.089E-04	-3.108E-03	-2.548E-02	-5.715E-02

CASE 17 INTERIOR ELECTRODE - + ⊕ - +

N| M->	0	1	2	3	4	5
0|	6.799E-02	7.657E-02	4.460E-02	9.785E-02	1.557E-01	3.692E-01
1|	2.670E-02	9.487E-02	1.156E-01	1.371E-01	3.520E-01	5.736E-01
2|	1.615E-03	1.141E-02	3.345E-02	7.091E-02	2.273E-01	4.131E-01
3|	7.919E-04	6.442E-03	2.066E-02	4.607E-02	1.548E-01	2.878E-01
4|	3.796E-05	4.538E-04	1.743E-03	7.529E-03	5.080E-02	1.098E-01
5|	1.869E-05	2.298E-04	8.785E-04	3.940E-03	2.766E-02	6.027E-02

CASE 18 INTERIOR ELECTRODE - + ⊕ + -

N| M->	0	1	2	3	4	5
0|	2.701E-02	6.475E-03	-5.500E-03	8.429E-03	-1.636E-02	3.011E-02
1|	0.0	0.0	0.0	0.0	0.0	0.0
2|	-2.197E-03	-1.127E-02	-1.490E-02	-1.635E-02	-4.910E-03	-1.760E-02
3|	0.0	0.0	0.0	0.0	0.0	0.0
4|	-5.548E-05	-6.346E-04	-2.118E-03	-4.910E-03	-6.400E-03	-1.166E-02
5|	0.0	0.0	0.0	0.0	0.0	0.0

CASE 19 INTERIOR ELECTRODE - + ⊕ + +

N| M->	0	1	2	3	4	5
0|	2.372E-02	4.379E-03	-5.944E-03	5.967E-03	-1.242E-02	2.214E-02
1|	-2.872E-03	-3.704E-03	4.665E-04	6.951E-04	-1.642E-04	-6.184E-04
2|	-2.191E-03	-1.064E-02	-1.422E-02	-1.326E-02	-1.278E-02	-1.182E-02
3|	7.946E-05	6.250E-04	1.906E-03	2.385E-03	3.296E-04	2.948E-03
4|	-4.428E-05	-4.222E-04	-1.658E-03	3.862E-03	-7.686E-03	-8.784E-03
5|	2.091E-06	2.492E-05	1.229E-04	3.803E-04	8.893E-04	1.403E-03

CASE 20 INTERIOR ELECTRODE + - ⊕ - +

N| M->	0	1	2	3	4	5
0|	1.015E-01	1.456E-01	1.007E-01	1.847E-01	3.332E-01	6.998E-01
1|	0.0	0.0	0.0	0.0	0.0	0.0
2|	6.118E-03	3.762E-02	9.205E-02	1.620E-01	4.727E-01	8.430E-01
3|	0.0	0.0	0.0	0.0	0.0	0.0
4|	1.458E-04	1.577E-03	6.121E-03	2.114E-02	1.133E-01	2.343E-01
5|	0.0	0.0	0.0	0.0	0.0	0.0

CASE 21 INTERIOR ELECTRODE + - ⊕ + +

N| M->	0	1	2	3	4	5
0|	5.801E-02	7.360E-02	4.905E-02	9.408E-02	1.627E-01	3.663E-01
1|	-3.041E-02	-9.928E-02	-1.098E-01	-1.370E-01	-3.510E-01	-5.748E-01
2|	2.332E-03	1.644E-02	4.086E-02	7.738E-02	2.324E-01	4.175E-01
3|	-6.795E-04	-5.605E-03	-1.819E-02	-4.237E-02	-1.506E-01	-2.839E-01
4|	6.009E-05	6.688E-04	2.600E-03	9.509E-03	5.449E-02	1.143E-01
5|	-1.612E-05	-1.994E-04	-7.301E-04	-3.492E-03	-2.644E-02	-5.881E-02

CASE 22 INTERIOR ELECTRODE + + ⊕ + +

N| M->	0	1	2	3	4	5
0|	2.046E-02	2.311E-03	-3.365E-03	4.598E-03	-1.047E-02	1.684E-02
1|	0.0	0.0	0.0	0.0	0.0	0.0
2|	-2.091E-03	-9.741E-03	-1.461E-02	-1.019E-02	-1.116E-02	-1.114E-02
3|	0.0	0.0	0.0	0.0	0.0	0.0
4|	-3.531E-05	-3.308E-04	-1.272E-03	-2.943E-03	-6.101E-03	-9.170E-03
5|	0.0	0.0	0.0	0.0	0.0	0.0

APPENDIX III

DETERMINATION OF CORRECT Y_{ij} ADMITTANCE COEFFICIENTS OF A TRANSDUCER WHEN THE CIRCUIT ELEMENTS jB_1 HAVE BEEN OMITTED IN INDIVIDUAL ELECTRODE CIRCUITS

In Section IV it was pointed out that it is not computationally feasible to calculate and store the data required to find the N elements jB_1 by numerical Hilbert transform for the N electrodes of a transducer.

By circuit analysis the admittance coefficients (y_{ij}) for the electrode portion of the circuit of Fig. 2 may be shown to be

$$y_{11} = y_{22} = -jZ_m \cot \Psi$$

$$y_{12} = jZ_m \csc \Psi$$

$$y_{13} = -j\frac{Y_m\beta}{2} \exp\left[-j(\Psi/2)\right]\left[(1 - j\cot\Psi)F(\beta) + j\csc\Psi F^*(\beta)\right]$$

$$y_{23} = -j\frac{Y_m\beta}{2} \exp\left[-j(\Psi/2)\right]\left[j\csc\Psi F(\beta) + (1 - j\cot\Psi)F^*(\beta)\right]$$

$$y_{33} = j\omega C + jB_1 + j\frac{\beta^2}{2}\left[\cot\frac{\Psi}{2}F_0^2(\beta) + \tan\frac{\Psi}{2}F_e^2(\beta)\right]$$

where $F(\beta)$ is the excitation function defined in Section II.

Suppose that the element jB_1 is omitted from the network (Fig. 2) for each electrode, then the only erroneous admittance coefficient for each electrode will be y_{33} (where port 3 is the electric port) since the element jB_1 is a pure shunt susceptance on port 3. Reference [3, appendix A] gives the recursion relations for finding the overall transducer admittance coefficients Y_{ij} from the single element coefficients $y_{ij}^{(k)}$, $k = 1,2,\cdots,N$, where the transducer consists of single elements interconnected as in Fig. 4. From these relations it is clear that the coefficients Y_{11}, Y_{12}, Y_{13}, Y_{22}, and Y_{23} do not depend on the $y_{33}^{(k)}$ and will thus be calculated correctly from the recursion relations even though the $y_{33}^{(k)}$ are in error. Only the coefficient Y_{33} will be in error and it may be determined as follows.

When the transducer radiates onto an infinite substrate, the acoustic ports of the equivalent circuit are terminated in the characteristic admittance G_0 as shown in Fig. 11. Under these conditions the input admittance at the electric port takes the form

$$Y_{\text{in}} = j\omega C + jB_a(f) + G_a(f)$$

$$= \underbrace{Y_{33}}_{\text{Imaginary}^5} + \underbrace{f(Y_{11},Y_{12},Y_{13},Y_{22},Y_{23},G_0)}_{\text{Complex}}.$$

The only erroneous term, Y_{33}, is purely imaginary and consists of the transducer capacitive susceptance ($j\omega C$—correct) as well as a contribution to $B_a(f)$ (incorrect because the elements jB_1 were omitted from the one-electrode circuits). In particular, the (real) radiation conductance $G_a(f)$ arises from the term $f(Y_{11},Y_{12},Y_{13},Y_{22},Y_{23},G_0)$ and is thus calculated correctly. We can therefore calculate the correct value of $B_a(f)$ as

$$B_a(f) = \mathcal{H}(G_a(f))$$

where $\mathcal{H}$ denotes the Hilbert transform, since the transduction is a causal process. Comparing the correct value of $B_a(f)$ so calculated against the erroneous value determined from the incomplete one-electrode networks yields the appropriate correction to Y_{33}. With all the Y_{ij} now correct, we have a complete description of the entire transducer. The correction term for Y_{33} may be added as a shunt susceptive element across the electrical port in the equivalent circuit for the entire transducer.

[5] Assuming that the transducer is internally lossless.

ACKNOWLEDGMENT

The authors wish to thank Dr. W. R. Jones and Dr. R. A. Dell-Imagine for useful discussions, and N. G. McKinney, C. R. Stout, F. M. Kandra, G. R. Scammon, and G. W. Judd for technical assistance.

REFERENCES

[1] W. R. Smith *et al.*, "Analysis of interdigital surface wave transducers by use of an equivalent circuit model," *IEEE Trans. Microwave Theory Tech. (Special Issue on Microwave Acoustics)*, vol. MTT-17, pp. 856–864, Nov. 1969.

[2] W. P. Mason, *Electromechanical Transducers and Wave Filters*, 2nd ed. Princeton, N.J.: Van Nostrand, 1948, pp. 201–209, 399–409.

[3] W. R. Smith, H. M. Gerard, and W. R. Jones, "Analysis and design of dispersive interdigital surface-wave transducers," *IEEE Trans. Microwave Theory Tech.*, vol. MTT-20, pp. 458–471, July 1972.

[4] R. H. Tancrell and M. G. Holland, "Acoustic surface wave filters," *Proc. IEEE*, vol. 59, pp. 393–409, Mar. 1971.

[5] C. S. Hartmann, D. T. Bell, Jr., and R. C. Rosenfeld, "Impulse model design of acoustic surface-wave filters," *IEEE Trans. Microwave Theory Tech. (Special Issue on Microwave Acoustic Signal Processing)*, vol. MTT-21, pp. 162–175, Apr. 1973.

[6] T. W. Bristol, W. R. Jones, P. B. Snow, and W. R. Smith, "Applications of double electrodes in acoustic surface wave design," in *Proc. 1972 IEEE Ultrasonics Symp.*, pp. 343–345.

[7] A. J. deVries, R. L. Miller, and T. J. Wojcik, "Reflection of a surface wave from three types of ID transducers," in *Proc. 1972 IEEE Ultrasonics Symp.*, pp. 353–358.

[8] H. Engan, "Excitation of elastic surface waves by spatial harmonics of interdigital transducers," *IEEE Trans. Electron Devices*, vol. ED-16, pp. 1014–1017, Dec. 1969.

[9] C. S. Hartmann and B. G. Secrest, "End effects in interdigital surface wave transducers," in *Proc. 1972 IEEE Ultrasonics Symp.*, pp. 413–416.

[10] R. Krimholtz, "Equivalent circuits for transducers having arbitrary asymmetrical piezoelectric excitation," *IEEE Trans. Sonics Ultrason.*, vol. SU-19, pp. 427–436, Oct. 1972.

[11] D. A. Leedom, R. Krimholtz, and G. L. Matthaei, "Equivalent circuits for transducers having arbitrary even- or odd-symmetry piezoelectric excitation," *IEEE Trans. Sonics Ultrason.*, vol. SU-18, pp. 128–141, July 1971.

[12] A. J. Bahr and R. E. Lee, "Equivalent circuit model for interdigital transducers with varying electrode widths," *Electron. Lett.*, vol. 9, pp. 281–282, June 28, 1973.

[13] G. L. Matthaei, D. Y. Wong, and B. P. O'Shaughnessy, "Simplifications for the analysis of interdigital surface-wave devices," *IEEE Trans. Sonics Ultrason.*, vol. SU-22, pp. 105–114, Mar. 1975.

[14] J. J. Campbell and W. R. Jones, "A method for estimating optimal crystal cuts and propagation directions for excitation of piezoelectric surface waves," *IEEE Trans. Sonics Ultrason.*, vol. SU-15, pp. 209–217, Oct. 1968.

[15] B. A. Auld and G. S. Kino, "Normal mode theory for acoustic waves and its application to the interdigital transducer," *IEEE Trans. Electron Devices*, vol. ED-18, pp. 898–908, Oct. 1971.

[16] A. J. Bahr, private communication.

[17] T. W. Bristol, "Synthesis of periodic unapodized surface wave transducers," in *Proc. 1972 IEEE Ultrasonics Symp.*, pp. 377–380.

[18] W. R. Smith, "Experimental distinction between crossed-field and in-line three-port circuit models for interdigital transducers," *IEEE Trans. Microwave Theory Tech.* (Short Papers), vol. MTT-22, pp. 960–964, Nov. 1974.

[19] R. C. M. Li and J. Melngailis, "The influence of stored energy at step discontinuities on the behavior of surface-wave gratings," *IEEE Trans. Sonics Ultrason.*, vol. SU-22, pp. 189–198, May 1975.